Metal–polymer hybrid nanomaterials for plasmonic ultrafast hydrogen detection

(article starts on next page)

Metal–polymer hybrid nanomaterials for plasmonic ultrafast hydrogen detection

Ferry A. A. Nugroho [1]*, Iwan Darmadi [1], Lucy Cusinato[1], Arturo Susarrey-Arce[1], Herman Schreuders[2], Lars J. Bannenberg[2], Alice Bastos da Silva Fanta[3], Shima Kadkhodazadeh [3], Jakob B. Wagner[3], Tomasz J. Antosiewicz [1,4], Anders Hellman[1], Vladimir P. Zhdanov[1,5], Bernard Dam [2] and Christoph Langhammer [1]*

Hydrogen–air mixtures are highly flammable. Hydrogen sensors are therefore of paramount importance for timely leak detection during handling. However, existing solutions do not meet the stringent performance targets set by stakeholders, while deactivation due to poisoning, for example by carbon monoxide, is a widely unsolved problem. Here we present a plasmonic metal–polymer hybrid nanomaterial concept, where the polymer coating reduces the apparent activation energy for hydrogen transport into and out of the plasmonic nanoparticles, while deactivation resistance is provided via a tailored tandem polymer membrane. In concert with an optimized volume-to-surface ratio of the signal transducer uniquely offered by nanoparticles, this enables subsecond sensor response times. Simultaneously, hydrogen sorption hysteresis is suppressed, sensor limit of detection is enhanced, and sensor operation in demanding chemical environments is enabled, without signs of long-term deactivation. In a wider perspective, our work suggests strategies for next-generation optical gas sensors with functionalities optimized by hybrid material engineering.

In a hydrogen economy[1] with hydrogen gas as a clean and sustainable energy carrier, hydrogen sensors will play a critical role due to hydrogen's wide flammability range in air. For safety reasons, any leaks in hydrogen energy storage systems, vehicles and appliances, as well as the entire hydrogen distribution infrastructure, must be detected immediately. Hence, hydrogen sensor performance targets specify a response time of 1 s at room temperature, across the concentration range from 0.1% to 10% (ref. [2]; see corresponding discussion in the Supplementary Information). In the quest to meet these challenging targets, optical nanoplasmonic hydrogen sensors based on hydride-forming metal nanoparticles have been introduced[3–7]. These are attractive because the optical signals generate no sparks and stem from absorption of hydrogen species into interstitial sites of the metal host, which renders such sensors intrinsically highly hydrogen-selective[3]. Furthermore, their optical fingerprint is spectrally tunable[4,8,9] and they can be miniaturized down to the single nanoparticle level[6,10,11]. In this field, like in many other hydrogen sensor platforms[12,13], Pd is the functional material of choice. This is due to its ability to dissociate hydrogen gas efficiently at ambient conditions and its reversible phase transformation from metal to metal hydride at room temperature[3,14], which gives rise to a sizable optical contrast[15]. However, among several other drawbacks, such as hysteretic behaviour[16] and response times falling short of the target value[13,17], the problem that hydrogen dissociation on Pd is effectively poisoned even by trace amounts of species like CO and NO$_2$ (refs. [17,18]) remains widely unsolved, in particular in combination with other critical sensor metrics (Supplementary Tables 1, 2 and 3). This is problematic because CO, for example, is omnipresent at ~0.2 ppm, and at even higher concentrations close to large point sources or in urban areas[19].

The plasmonic metal–polymer optical hydrogen sensor platform presented here overcomes all these long-standing limitations by capitalizing on generic and synergistic effects that arise from combining PdAu alloy plasmonic nanoparticle signal transducers with tailored thin polymer membrane layers (Fig. 1a). As we show, the stringent 1 s room-temperature response time target can be met by tailoring the nanoparticle volume-to-surface ratio in concert with a reduction of the apparent activation energy by engineering the metal–polymer interface. Simultaneously, hysteresis is suppressed, the sensor limit of detection (LoD) is significantly enhanced and sensor operation in demanding chemical environments without any signs of deactivation, even after 4 months, is enabled.

Plasmonic metal–polymer optical hydrogen sensor platform

The nanoarchitecture of our hybrid sensor consists of a nanofabricated quasi-random array of hydride-forming and plasmonically active metal nanoparticles on a glass substrate coated with a thin polymeric film (Fig. 1a,b). Specifically, we chose a Pd$_{70}$Au$_{30}$ alloy, as well as a pure Pd control. The chosen alloy composition is optimal because, at a lower Au fraction, sensor accuracy is compromised by hysteresis[20,21] (that is, the readout is non-specific as it depends on the hydrogen pressure history), while at a higher Au fraction the sensitivity is reduced[4,22]. We nanofabricated the alloy and Pd nanostructures with average particle dimensions of 190 nm (diameter) and 25 nm (height) according to the 'hole-mask colloidal lithography' method since particles of this size are structurally very stable and exhibit a distinct plasmon-related light-absorption peak. Subsequent depositions of the metal constituents matching the targeted composition were followed by high-temperature annealing to induce alloy formation[21]. This approach yields

[1]Department of Physics, Chalmers University of Technology, Göteborg, Sweden. [2]Department of Chemical Engineering, Delft University of Technology, Delft, the Netherlands. [3]Center for Electron Nanoscopy, Technical University of Denmark, Kongens Lyngby, Denmark. [4]Faculty of Physics, University of Warsaw, Warsaw, Poland. [5]Boreskov Institute of Catalysis, Russian Academy of Sciences, Novosibirsk, Russia. *e-mail: ferryn@chalmers.se; clangham@chalmers.se
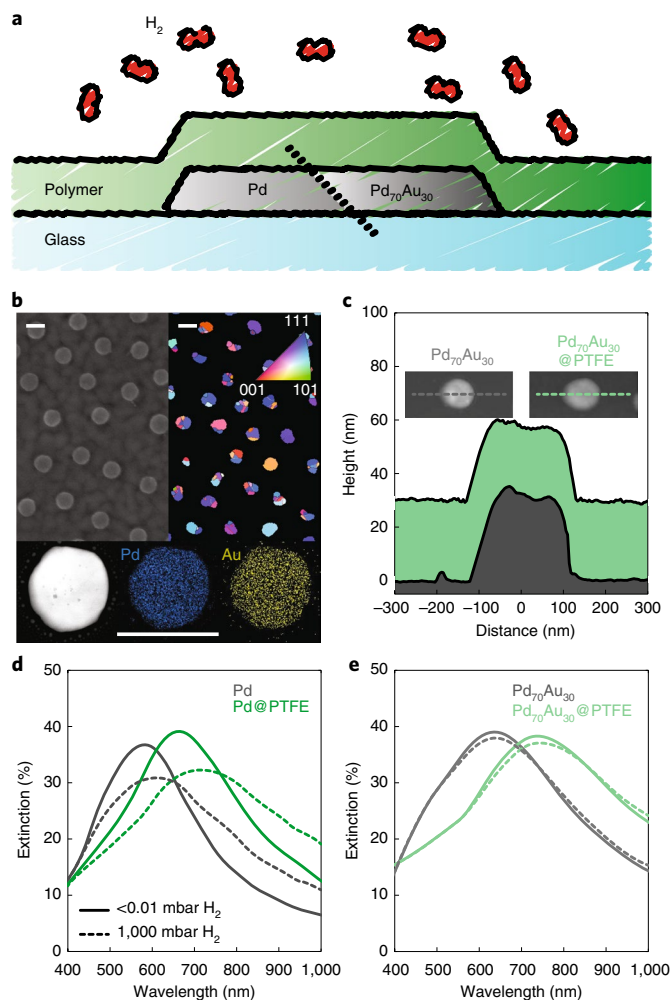
Fig. 1 | Plasmonic metal–polymer hybrid nanomaterial architecture and characterization. a, Artist's rendition of a plasmonic metal–polymer nanomaterial comprising hydride-forming Pd or $Pd_{70}Au_{30}$ alloy nanoparticles and a thin polymer coating. **b**, Scanning electron microscopy (SEM) image (top left) and transmission Kikuchi diffraction (TKD) micrograph (top right) of a $Pd_{70}Au_{30}$ nanoparticle array, and energy-dispersive X-ray elemental maps of an individual $Pd_{70}Au_{30}$ alloy nanoparticle (bottom). The colour code for the TKD images is explained in the inverse pole figure plot, which depicts the bulk grain crystallographic orientation with respect to the out-of-plane axis. Scale bars, 200 nm. **c**, Atomic force microscopy (AFM) image of an individual $Pd_{70}Au_{30}$ alloy particle before and after PTFE coating. The profile of the coated particle is shifted upward by the nominal 30 nm PTFE thickness for clarity. Optical extinction spectra of a (**d**) Pd and (**e**) $Pd_{70}Au_{30}$ alloy nanoparticle array before and after PTFE coating, measured in vacuum and at 1,000 mbar H_2.

homogeneously alloyed polycrystalline disk-shaped nanoparticles[4,21] with a narrow size distribution (Fig. 1b, Supplementary Figs. 1 to 6 and Supplementary Table 4).

As the first polymer coating we chose polytetrafluoroethylene (PTFE) because of its high chemical resistance and hydrophobicity. Radiofrequency sputtering of a 30 nm thin layer from a PTFE target yielded a conformal coating of the entire nanoparticle array (Fig. 1c and Supplementary Figs. 7 and 8). The optical extinction spectra of the $Pd_{70}Au_{30}$ and Pd systems are shown before and after applying the PTFE coating in Fig. 1d,e, which feature a localized surface plasmon resonance (LSPR) peak that broadens and shifts to the red after PTFE deposition due to the high refractive index of the coating[23].

Following exposure to 1,000 mbar of hydrogen, this peak further broadens and redshifts due to the change in both volume and permittivity of the metal nanoparticles induced by hydrogen population of the interstitial lattice sites[15]. This LSPR peak shift, $\Delta\lambda_{peak}$, which is a linear function of the hydrogen concentration inside the nanoparticles expressed as the H/Pd ratio[22], then serves as the basis for our nanoparticle–polymer hybrid optical hydrogen sensors.

Accuracy and LoD of the sensor@PTFE
As the first characterization of our sensors we measured optical hydrogen absorption and desorption isotherms at 30 °C for pure Pd and the $Pd_{70}Au_{30}$ alloy in the absence and presence of the 30 nm PTFE coating (Fig. 2a,b). For Pd, a characteristic α-phase region at low hydrogen partial pressure is observed, where hydrogen is diluted at low concentration in solid solution. At a critical hydrogen pressure, the α + β phase coexistence region (plateau) at the first-order phase transition to and from the hydride (β-phase) appears and exhibits hysteresis. Finally, the pure β-phase region at high hydrogen partial pressure is observed[24]. In contrast, the $Pd_{70}Au_{30}$ system exhibits a monotonous hysteresis-free response. Interestingly, adding the PTFE coating to the two sensors not only retains the identified beneficial properties of the $Pd_{70}Au_{30}$ alloy but also enhances the signal amplitude by a factor of approximately two throughout the entire pressure range investigated. This is remarkable because, as becomes clear from quartz-crystal microbalance (QCM) measurements, this enhancement is not caused by hydrogen absorption in the PTFE itself (Fig. 2c,d). Specifically, our analysis indicates that the same amount of hydrogen is absorbed with and without PTFE coating both for Pd and the $Pd_{70}Au_{30}$ (the absolute numbers expressed as H/Pd ratio are in good agreement with earlier reports[20,25]), corroborating that hydrogen only interacts with the nanoparticles. Furthermore, our density functional theory (DFT) calculations show that the interaction between H_2 and PTFE (and poly(methylmethacrylate) (PMMA)) consists of only weak dispersion forces (Supplementary Fig. 11).

These results contrast with earlier work reporting on nearly doubled hydrogen solubility in metal–organic framework-coated Pd nanoparticles[26]. To address this in more detail, we note that the sensitivity of a plasmonic hydrogen sensor is dictated by the spectral position of the plasmonic resonance, λ_{peak}, in the non-hydrogenated state[22]. Adding a polymer coating spectrally redshifts λ_{peak} (cf. Fig. 1d,e), so we expect an increase in sensitivity. This is indeed the case and the reason for the observed enhancement of the signal amplitude, as we discuss in detail in the Supplementary Information based on finite-difference–time-domain (FDTD) simulations. Because this enhancement is a purely optical far-field effect (the concentration of absorbed hydrogen remains the same), it is generic to any (polymer) coating and can be maximized by a high refractive index of the latter and/or by increasing its thickness (Supplementary Figs. 16 and 17) at the cost of a slight reduction in the figure-of-merit of the plasmonic sensor readout (Supplementary Fig. 18). At the same time it is exclusive to plasmonic hydrogen sensors based on nanoparticles because no such optical signal enhancement was observed for PTFE-coated Pd thin films[27]. Finally, we also note that the observed symmetric lowering of the plateau pressures for the Pd@PTFE system (Fig. 2a,c) hints at strain imposed by the PTFE layer[28] (for related estimates, see Supplementary Information).

The LoD of the Pd@PTFE and $Pd_{70}Au_{30}$@PTFE sensors is derived by exposing them to pulses of gradually decreasing H_2 pressure in vacuum (from 1,000 to 7 μbar, the lowest pressure attainable in our set-up) and by measuring the $\Delta\lambda_{peak}$ at 1 Hz sampling frequency (Fig. 2e). Defining the LoD as 3σ, where σ is the noise of the acquired signal (that is, 0.01 nm; see Supplementary Figs. 20 and 21 and corresponding discussion), we extrapolate that the LoD is <5 μbar in pure hydrogen (Fig. 2f). To assess the sensitivity under more realistic conditions, we conducted similar experiments for
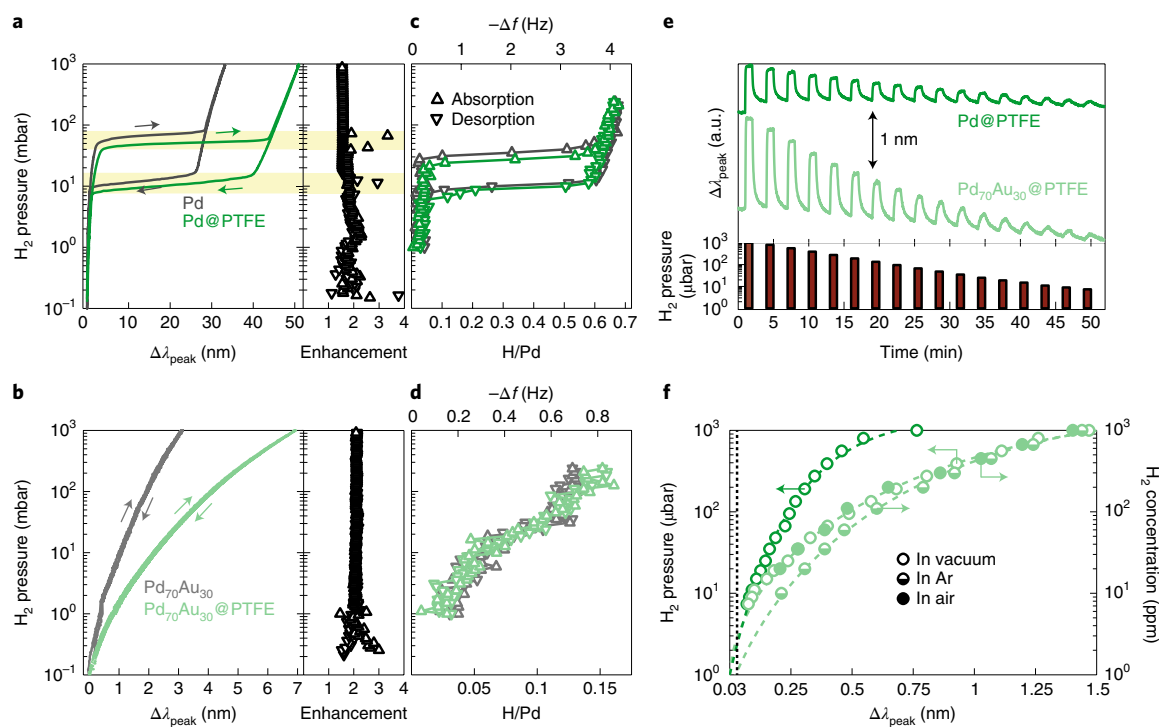
Fig. 2 | Sensitivity enhancement and LoD of Pd@PTFE and Pd$_{70}$Au$_{30}$@PTFE. a,b, Optical absorption and desorption isotherms of Pd (**a**) and Pd$_{70}$Au$_{30}$ alloy (**b**) sensors before and after PTFE coating. Arrows denote the sorption direction. The panels to the right show the $\Delta\lambda_{peak}$ ratio of the coated and uncoated sensors. **c,d,** Pressure–composition isotherms of Pd (**c**) and Pd$_{70}$Au$_{30}$ (**d**) sensors before and after PTFE coating measured by QCM. The hydrogen concentration in the metal, expressed as H/Pd, is in excellent agreement with previous reports[20], and no H$_2$ is absorbed in the PTFE itself due to the identical response by the coated and uncoated system. **e,** $\Delta\lambda_{peak}$ response to stepwise decreasing H$_2$ pressure in the 7–1,000 µbar range, measured at 1 Hz sampling frequency in a vacuum chamber. **f,** Measured $\Delta\lambda_{peak}$ as a function of H$_2$ pressure derived from **e** and from measurements in Ar and synthetic air background (Supplementary Figs. 25 and 26). Green dashed lines show extrapolation from the lowest reliably attainable data point in our system for the Ar and air background to the 3σ point, indicating a LoD < 1 ppm and 5 ppm, respectively. The black dashed line marks the extrapolated LoD at $3\sigma = 0.03$ nm. All experiments were performed at 30 °C.

the Pd$_{70}$Au$_{30}$@PTFE sensor in Ar and in synthetic air carrier gas at atmospheric pressure in a flow reactor set-up. In both backgrounds, down to the lowest H$_2$ concentration experimentally attainable, that is, 10 ppm and 20 ppm, respectively, a $\Delta\lambda_{peak}$ response is clearly discernible. This places our system among the most sensitive hydrogen sensors reported so far under simulated application conditions in air[29,30], notably with significant potential to further enhance the sensitivity by, for example, tailoring the coating layer material and its thickness, and by optimizing the nanoparticle dimensions[22]. To this end, by extrapolating the LoD based on the experimentally derived noise in flow conditions (Supplementary Fig. 24) we derive an LoD of 1 ppm in Ar and 5 ppm in synthetic air.

Response time of the sensor@PTFE
We next measured the response times of uncoated and PTFE-coated Pd and Pd$_{70}$Au$_{30}$ alloy sensors at 30 °C by monitoring their temporal response to a stepwise increase/decrease of hydrogen pressure to/from 40 mbar H$_2$ (that is, the lower flammability limit) in a vacuum chamber (Fig. 3a,b; see Supplementary Fig. 27 for recovery times). We observe two key effects: (1) for both absorption and desorption the response time of the uncoated Pd$_{70}$Au$_{30}$ sensor is significantly shorter than for the uncoated Pd one; (2) the PTFE coating for both systems further shortens the response time to significantly below 1 s for the alloy. The detailed quantitative analysis of the Pd and Pd$_{70}$Au$_{30}$ absorption and desorption kinetics via Arrhenius analysis (Supplementary Figs. 28 and 29) reveals a significant reduction in the apparent activation energies, E_a, for both hydrogen absorption and desorption. This is due to the PTFE coating

(Fig. 3d,e and Supplementary Figs. 28 and 29), which also refines the understanding of the observed hydrogen sorption kinetics acceleration in PTFE-coated Pd thin films reported in ref. [27]. These results, along with similar kinetics acceleration observed for metal–organic framework-coated Pd sensors measured in vacuum/hydrogen[26] and in air[31], imply that the kinetics-accelerating effect of such coatings may be generic. To this end, a number of different explanations of the origin of the accelerated kinetics is given in the literature, such as the modification of surface chemical[27,32] and electronic states[26,27,33], physical force/stress imposed by the coating layer[33] and the removal of competing molecules reacting on the surface[31].

Employing DFT calculations to capture the experimentally observed trends, we show that the measured decrease in E_a induced by the polymer coating is connected to the absorption and desorption processes at the nanoparticle–polymer interface (Fig. 3e; see Supplementary Figs. 12 and 13 for the modelled Pd@PTFE system), mediated by polymer–metal bond formation verified by X-ray photoelectron spectroscopy (XPS) analysis (Supplementary Figs. 9 and 10). On the one hand, the activation barrier for hydrogen absorption from surface to subsurface sites is reduced by 11 kJ mol^{-1} due to coating with PTFE, resulting in faster absorption. On the other hand, for sites close to the PTFE, surface-adsorbed hydrogen is destabilized by 9 kJ mol^{-1}, which leads to faster H$_2$ desorption. These effects give rise to a reduction of E_a for both hydrogen absorption and desorption, explaining the experimentally observed accelerated kinetics and measured lower apparent activation barriers for the respective rate-limiting step. Concerning the kinetics, we also note that the dependence of the response time on pressure (Fig. 3g and
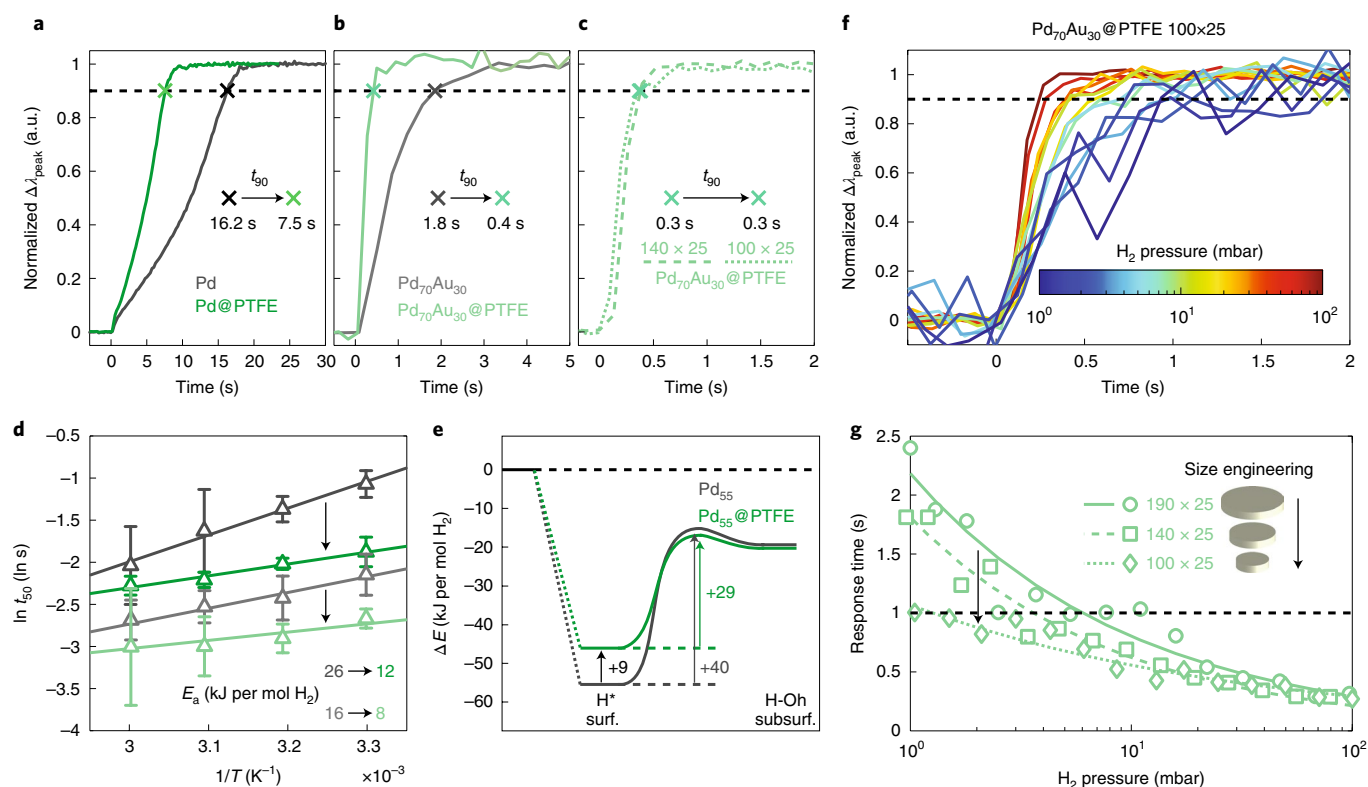
Fig. 3 | Response times of Pd@PTFE and Pd$_{70}$Au$_{30}$@PTFE at room temperature. a,b, Accelerated absorption kinetics to 40 mbar H$_2$ are observed for PTFE-coated Pd (**a**) and Pd$_{70}$Au$_{30}$ (**b**) sensors with 190 × 25 nm^2 average nanoparticle dimensions. t_{90} is the response time defined as the time to reach 90% of the total signal and is marked by black dashed lines. **c**, Engineering the volume-to-surface ratio by using nanoparticles with smaller dimensions enables faster absorption kinetics, as shown for 140 × 25 nm^2 and 100 × 25 nm^2 Pd$_{70}$Au$_{30}$@PTFE sensors. **d**, Measured apparent hydrogen absorption activation energies, E_a, of a Pd and Pd$_{70}$Au$_{30}$ sensor before and after PTFE coating, revealing a distinct reduction of E_a with the PTFE coating. Error bars represent the s.d. from three measurements. **e**, DFT calculations of the energy landscape for hydrogen absorption, either adsorbed on the surface (H* surf.) or adsorbed in a subsurface octahedral site (H-Oh subsurf.) in Pd55, with and without PTFE adsorbed on the surface. The reference is taken as Pd$_{55}$ + 1/2H$_2$(g) and Pd$_{55}$@PTFE + 1/2H$_2$(gas phase), respectively. **f**, 100 × 25 nm^2 Pd$_{70}$Au$_{30}$@PTFE sensor response to H$_2$ pressure pulses in the range from 100 to 1 mbar. **g**, Response time of Pd$_{70}$Au$_{30}$@PTFE sensors of different sizes to varying H$_2$ pressure pulses. For the 100 × 25 nm^2 sensor, a sub-second response is achieved throughout the investigated pressure range down to 1 mbar, making this the fastest hydrogen sensor ever reported under these conditions (Supplementary Table 2). The lines denote a power-law fit based on Supplementary equation (18). The raw data for 190 × 25 nm^2 and 140 × 25 nm^2 sensors are shown in Supplementary Fig. 30.

Figs. 4e and 5c) is fairly weak and close to the power-law form with a small exponent (cf. Supplementary equation (15)), indicating energetic heterogeneity at the surface of the alloy (see the corresponding discussion in the Supplementary Information).

Having established that the hydrogen absorption rate into the bulk of the nanoparticle sensors is limited by their surface[34], the timescale is expected to be proportional to the volume-to-surface area ratio, with the proportionality constant depending on the specifics of the kinetics at the surface (Supplementary Figs. 32 to 36 and the corresponding discussion). Hence, as a key advantage enabled by a sensor platform based on nanoparticles, tailoring the volume-to-surface ratio should provide a faster response. Indeed, reducing the mean diameter of the nanoparticles in a Pd$_{70}$Au$_{30}$@PTFE sensor from 190 nm to 100 nm further reduces the response time for desorption from ~9 s to 3 s (Supplementary Fig. 27) and for absorption to (below) the resolution limit of our system at 0.3 s (Fig. 3c). Hence, the 100 × 25 nm^2 Pd$_{70}$Au$_{30}$@PTFE sensor meets the toughest of the US DoE targets[2], defined as a response time of <1 s to 1 mbar hydrogen at ambient temperature (Fig. 3f,g). Furthermore, a recovery time of below 5 s throughout the same hydrogen pressure range is also achieved (Supplementary Fig. 31), which represents the current state of the art in this respect. Additionally, we highlight that downsizing and volume-to-surface area engineering of the

nanostructures offers the potential to further improve these already impressive response times, in particular when using optimized nanoparticle designs, such as nanorods, that combine a spectrally redshifted LSPR for optimized LoD with small volume-to-surface area ratio. However, on utilizing the PTFE coating as a selective membrane to prevent sensor deactivation by trace gases present in air, such as CO and NO$_2$, we find that sufficient protection is not obtained, as evidenced by deactivation tests carried out in synthetic air carrier gas to mimic real application conditions (Supplementary Fig. 48; 10 cycles of 4% H$_2$ followed by 10 cycles of 4% H$_2$ plus an interfering gas: 3% CO$_2$, 0.5% CH$_4$, 0.1% CO, 0.05% NO$_2$).

Pd$_{70}$Au$_{30}$@PMMA sensor

To overcome the shortcomings of the PTFE coating, in the second part of our study we investigated an alternative polymer system—PMMA—for which excellent H$_2$ selectivity to other gases has been demonstrated[35–37]. To assess the molecular sieving function of the PMMA coating, we spin-coated a 35-nm-thick PMMA film onto a 190 × 25 nm^2 Pd$_{70}$Au$_{30}$ sensor (for a neat Pd@PMMA analogue and raw data see Supplementary Figs. 37 to 40). The corresponding Pd$_{70}$Au$_{30}$@PMMA sensor response in an identical deactivation test as described above is summarized in Fig. 4a, which shows the excellent protection provided by the PMMA layer. Specifically,
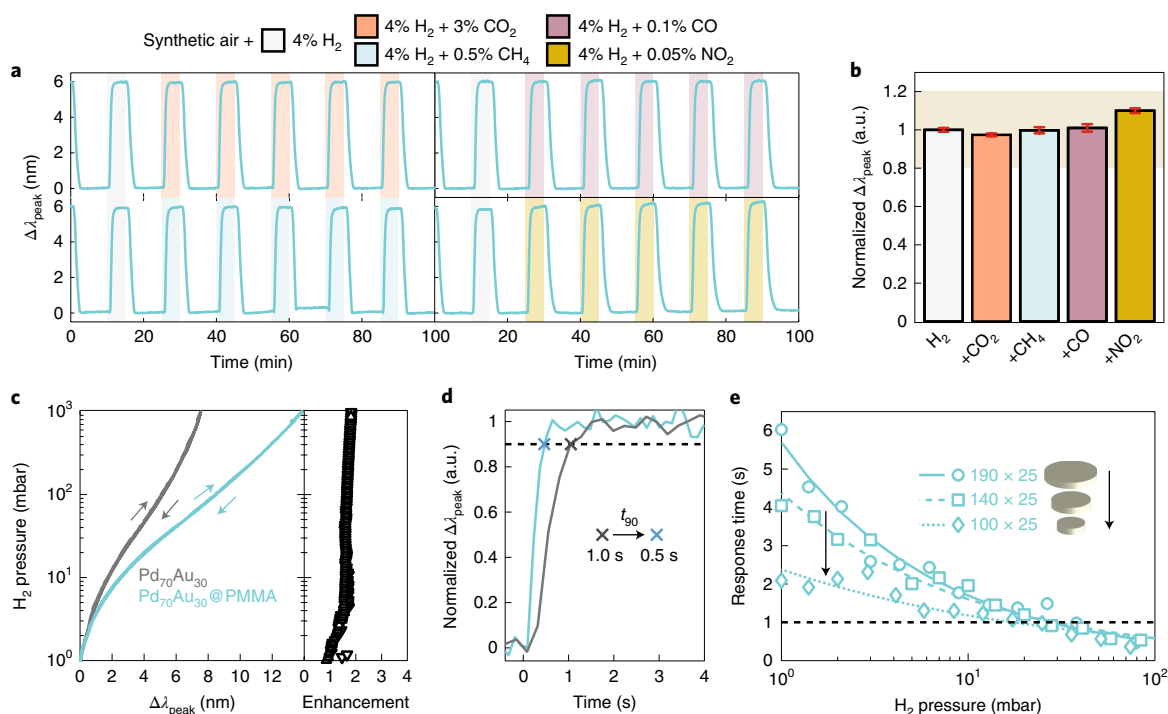
Fig. 4 | Pd$_{70}$Au$_{30}$@PMMA sensor. a, Time-resolved $\Delta\lambda_{peak}$ response of Pd$_{70}$Au$_{30}$@PMMA to a pulse of 4% H$_2$ followed by five pulses of, respectively, 4% H$_2$ and 3% CO$_2$, 4% H$_2$ and 0.5% CH$_4$, 4% H$_2$ and 0.1% CO, and 4% H$_2$ and 0.05% NO$_2$ in synthetic air carrier gas, measured at atmospheric pressure. **b**, The $\Delta\lambda_{peak}$ signals are retained throughout exposure to the different background gases, as summarized here, where the respective signals are normalized to the signal obtained in pure 4% H$_2$. Error bars denote s.d. from 10 cycles. The shaded area indicates the $\pm20\%$ deviation limit from the normalized $\Delta\lambda_{peak}$ in pure 4% H$_2$. **c**, Optical absorption and desorption isotherms of the Pd$_{70}$Au$_{30}$ sensor measured before and after adding the PMMA coating. Arrows denote the sorption direction. The panel to the right depicts the $\Delta\lambda_{peak}$ ratio of the coated and uncoated sensors, revealing a similar signal enhancement factor to the one found for the PTFE-coated system (see Fig. 2b). For the higher $\Delta\lambda_{peak}$ observed here, see Supplementary Fig. 43 and corresponding discussion. **d**, Pd$_{70}$Au$_{30}$ sensor response before and after PMMA coating to a stepwise H$_2$ pressure increase to 40 mbar. **e**, Response times to different H$_2$ pressure pulses of Pd$_{70}$Au$_{30}$@PMMA sensors with different nanoparticle sizes. The lines denote a power-law fit based on Supplementary equation (18). All experiments were performed at 30 °C.

as depicted in Fig. 4b, the sensor signal for all interfering gases is retained (with a significant margin) within the $\pm20\%$ deviation limit from the normalized $\Delta\lambda_{peak}$ in pure 4% H$_2$ according to the performance standard for hydrogen sensors[38]. This is remarkable in view of the strong deactivation of the uncoated control (Supplementary Fig. 48) by, for example, CO through effective poisoning of the surface via strong CO chemisorption and the concurrent blocking of hydrogen dissociation sites[18].

Referring to the beneficial effects of the PTFE coating on the sensor performance identified above, we find that the same signal amplitude enhancement by a factor of approximately two is also observed for PMMA (Fig. 4c). Hence, as anticipated and discussed above, this is indeed a generic effect inherent to dielectric (polymer) coatings. The observed similar magnitude of the enhancement with PTFE and PMMA is thus solely the consequence of their similar refractive indices and the essentially identical thicknesses of the coatings, because for PMMA it is also the case that no relevant hydrogen sorption occurs within the polymer itself (Supplementary Fig. 11). In terms of response time shortening, our analysis reveals that this effect is also present for a PMMA coating, as the response time to 40 mbar H$_2$ for the Pd$_{70}$Au$_{30}$@PMMA sensor is reduced to 0.5 s (Fig. 4d). However, the acceleration of the hydrogen sorption kinetics is, on average, a factor of two smaller for PMMA compared to PTFE and thus, even by reducing the nanoparticle diameter to 100 nm, the system falls slightly short of the DoE target for a sub-second response to 1 mbar at room temperature (Fig. 4e). The reason for this is the smaller reduction of E_a of the rate-limiting steps

during hydrogen absorption and desorption induced by PMMA, compared to PTFE (Supplementary Figs. 41 and 42), as also confirmed by DFT calculations (Supplementary Figs. 14 and 15).

Pd$_{70}$Au$_{30}$@PTFE/PMMA tandem sensor

As an intermediate conclusion it becomes clear that the ideal polymer layer would essentially combine the properties of the evaluated PTFE and PMMA systems. Hence, we fabricated a Pd$_{70}$Au$_{30}$ hydrogen sensor encapsulated by a tandem 30 nm PTFE + 35 nm PMMA structure. In this way we were able to test the hypotheses that (1) it is indeed the PTFE–nanoparticle interface and the corresponding reduction of the apparent activation barriers that gives rise to the superior response time, (2) PMMA functions as a superior molecular sieve layer and (3) these two functions can be combined in a heterostructure. To prepare the sensor we applied a 5 s H$_2$ plasma treatment to the previously tested Pd$_{70}$Au$_{30}$@PTFE sensor (Figs. 1, 2 and 3) to render the PTFE surface hydrophilic[39]. This enabled wetting and thus spin-coating of PMMA dissolved in methoxybenzene solvent. The obtained polymer tandem structure is depicted schematically in Fig. 5a, together with a cross-sectional SEM micrograph in which a PdAu alloy nanoparticle encapsulated in the tandem polymer arrangement is clearly resolved. The effective coating of the PTFE layer by the PMMA was further confirmed by XPS analysis (Fig. 5b).

Assessment of the room-temperature response time for the tandem coating revealed that it is essentially identical to that with the PTFE coating alone (Fig. 5c). Since we used the same sensor in both
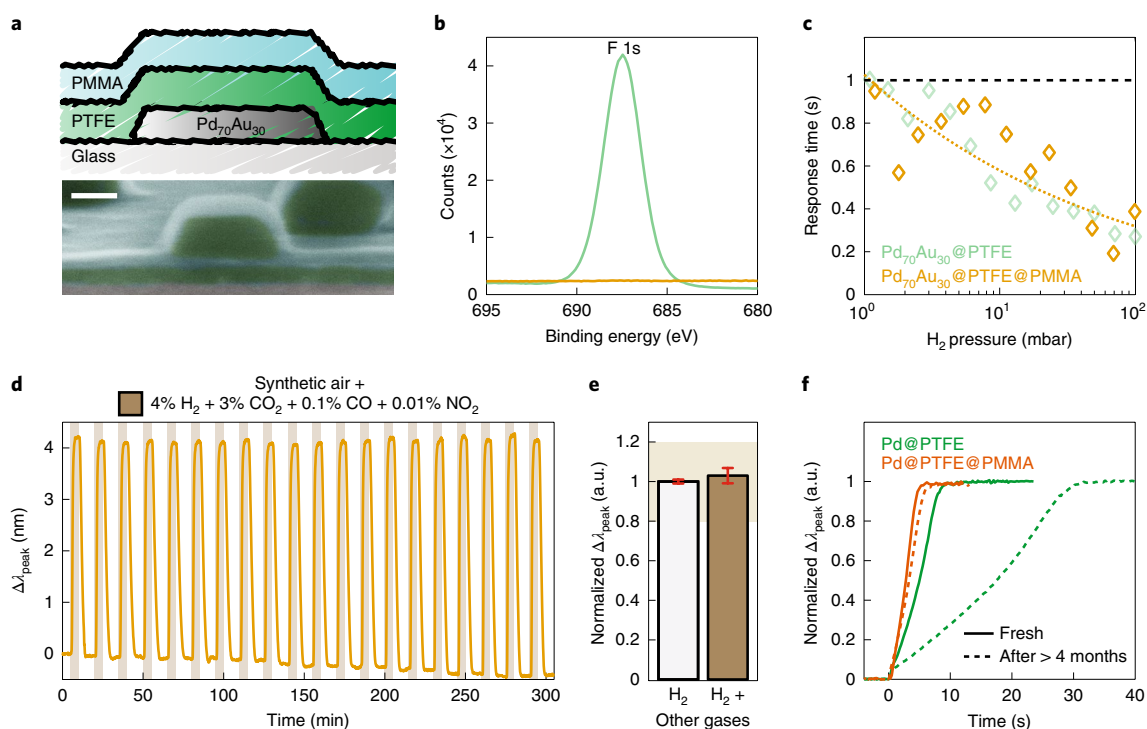
Fig. 5 | Pd₇₀Au₃₀@PTFE@PMMA tandem sensor. $Pd_{70}Au_{30}$@PTFE@PMMA tandem sensor. **a**, Top, artist's rendition of a tandem sensor comprising a heterostructure polymer coating on an alloy nanoparticle array. Bottom, cross-sectional SEM image of the sensor, revealing the polymer layers with different contrast. Scale bar, 100 nm. **b**, XPS spectra of the F 1s peak of a $Pd_{70}Au_{30}$@PTFE and a $Pd_{70}Au_{30}$@PTFE@PMMA tandem sensor. The absence of the F 1s peak for the tandem confirms coating of the PTFE by PMMA. **c**, Response times of a 100×25 nm² tandem sensor to different H_2 pressure pulses (raw data are provided in Supplementary Fig. 44), plotted with those of the same sensor with PTFE coating only (cf. Fig. 3g). The dashed orange line denotes a power-law fit based on Supplementary equation (18). **d**, $\Delta\lambda_{peak}$ of the tandem sensor for 20 cycles of 4% H_2 plus 3% CO_2, 0.1% CO and 0.05% NO_2 in synthetic air. **e**, Corresponding $\Delta\lambda_{peak}$ normalized to $\Delta\lambda_{peak}$ in pure 4% H_2, revealing the excellent deactivation resistance of the tandem. Error bars denote s.d. from 20 cycles. The shaded area indicates the ±20% deviation limit from the normalized $\Delta\lambda_{peak}$ in pure 4% H_2. **f**, Absorption kinetics of Pd@PTFE and Pd@PTFE@PMMA sensors to 40 mbar H_2 at different aging states.

cases, the reproducibility is remarkable. Furthermore (and as the key result), the subsecond response is again retained down to 1 mbar, meeting the DoE target. Comparing the E_a for the two systems, we found them to be identical (Supplementary Fig. 45), corroborating that the kinetics acceleration observed is indeed governed solely by the direct interaction between the coating material and nanoparticle surface. At the same time, the deactivation tests in synthetic air revealed that the same deactivation resistance is achieved as for the PMMA alone (Supplementary Fig. 48). Moreover, in a significantly exaggerated test to mimic the concentrations in an urban environment, the sensor with the tandem coating shows no sign of deactivation when exposed to twenty 4% H_2 pulses mixed with 3% CO_2, 0.1% CO and 0.01% NO_2 (Fig. 5d). In this tough test, the absolute response also remains well within the ±20% deviation limit according to the performance standard for hydrogen sensors[38] (Fig. 5e). This excellent deactivation resistance is also retained in the long term. In particular, after four months of exposure to ambient conditions, the tandem sensor retains its response, while the PTFE-only-coated sensor is significantly deactivated (indicated by the drastically reduced response time; Fig. 5f). Finally, as an additional advantage of the tandem system arising due to its doubled polymer layer thickness, its sensitivity is further enhanced by 30% compared to that with the PTFE layer alone (Supplementary Figs. 46 and 47), in agreement with our FDTD simulations (Supplementary Fig. 17).

Discussion

The concerted hydrogen sorption rate and sensitivity enhancement (as well as molecular sieving effects) we find for polymer coating layers on hydride-forming metal nanoparticles provide a mechanism by which plasmonic nanoparticle arrays can operate as optical hydrogen sensors with unprecedented response metrics. The performances of the plasmonic metal–polymer optical hydrogen sensors presented here challenge existing hydrogen-sensing technologies (Supplementary Table 2) and meet for the first time the stringent 1 s response time target at ambient temperature and 1 mbar H_2 partial pressure. This breakthrough is achieved by combining two key effects: (1) reducing the activation barrier for surface-to-subsurface hydrogen diffusion via polymer–metal surface bond formation and (2) tailoring the volume-to-surface area ratio, a feature uniquely possible in nanoparticles, to overcome the intrinsic response time limitations imposed by the identified surface-associated rate-limiting steps during (de)hydrogenation of the sensor. The latter point also implies that it is fundamentally impossible to reach the 1 s response time target at low hydrogen partial pressures with macroscopic (bulk) or, to some extent, thin-film systems (see corresponding discussion in the Supplementary Information) based on Pd and its alloys, because in this regime the volume-to-surface area ratio is the critical factor determining the response time. In a wider perspective, our work thus opens the door to next-generation (optical) gas sensors centred on the idea of a hybrid material that combines tailored plasmonic signal transducers with multiple selective membrane materials, which, by engineering the dimensions and interfaces of the material constituents, enable the optimization of sensitivity, selectivity, deactivation resistance and response times to meet the ever increasing demand for advanced sensor technologies.

Online content

Any methods, additional references, Nature Research reporting summaries, source data, statements of data availability and associated accession codes are available at https://doi.org/10.1038/s41563-019-0325-4.

References

1. Hydrogen to the rescue. *Nat. Mater.* **17**, 565 (2018).
2. U.S. Department of Energy, Energy Efficiency and Renewable Energy (EERE), Fuel Cell Technologies Office. *Multi-Year Research, Development, and Demonstration Plan, 2011–2020. Section 3.7 Hydrogen Safety, Codes and Standards* (EERE, 2015).
3. Wadell, C., Syrenova, S. & Langhammer, C. Plasmonic hydrogen sensing with nanostructured metal hydrides. *ACS Nano* **8**, 11925–11940 (2014).
4. Wadell, C. et al. Hysteresis-free nanoplasmonic Pd–Au alloy hydrogen sensors. *Nano Lett.* **15**, 3563–3570 (2015).
5. Yip, H. K. et al. Gold nanobipyramid-enhanced hydrogen sensing with plasmon red shifts reaching ≈140 nm at 2 vol% hydrogen concentration. *Adv. Opt. Mater.* **5**, 1700740 (2017).
6. Liu, N., Tang, M. L., Hentschel, M., Giessen, H. & Alivisatos, A. P. Nanoantenna-enhanced gas sensing in a single tailored nanofocus. *Nat. Mater.* **10**, 631–636 (2011).
7. Tittl, A. et al. Palladium-based plasmonic perfect absorber in the visible wavelength range and its application to hydrogen sensing. *Nano Lett.* **11**, 4366–4369 (2011).
8. Langhammer, C., Zorić, I., Kasemo, B. & Clemens, B. M. Hydrogen storage in Pd nanodisks characterized with a novel nanoplasmonic sensing scheme. *Nano Lett.* **7**, 3122–3127 (2007).
9. Sterl, F. et al. Magnesium as novel material for active plasmonics in the visible wavelength range. *Nano Lett.* **15**, 7949–7955 (2015).
10. Baldi, A., Narayan, T. C., Koh, A. L. & Dionne, J. A. In situ detection of hydrogen-induced phase transitions in individual palladium nanocrystals. *Nat. Mater.* **13**, 1143–1148 (2014).
11. Syrenova, S. et al. Hydride formation thermodynamics and hysteresis in individual Pd nanocrystals with different size and shape. *Nat. Mater.* **14**, 1236–1244 (2015).
12. Favier, F., Walter, E. C., Zach, M. P., Benter, T. & Penner, R. M. Hydrogen sensors and switches from electrodeposited palladium mesowire arrays. *Science* **293**, 2227–2231 (2001).
13. Penner, R. M. A nose for hydrogen gas: fast, sensitive H₂ sensors using electrodeposited nanomaterials. *Acc. Chem. Res.* **50**, 1902–1910 (2017).
14. Adams, B. D. & Chen, A. The role of palladium in a hydrogen economy. *Mater. Today* **14**, 282–289 (2011).
15. Poyli, M. A. et al. Multiscale theoretical modeling of plasmonic sensing of hydrogen uptake in palladium nanodisks. *J. Phys. Chem. Lett.* **3**, 2556–2561 (2012).
16. Schwarz, R. B. & Khachaturyan, A. G. Thermodynamics of open two-phase systems with coherent interfaces: application to metal–hydrogen systems. *Acta Mater.* **54**, 313–323 (2006).
17. Hübert, T., Boon-Brett, L., Black, G. & Banach, U. Hydrogen sensors—a review. *Sens. Actuat. B* **157**, 329–352 (2011).
18. Palmisano, V. et al. Selectivity and resistance to poisons of commercial hydrogen sensors. *Int. J. Hydrogen Energy* **40**, 11740–11747 (2015).
19. Clerbaux, C. et al. Carbon monoxide pollution from cities and urban areas observed by the Terra/MOPITT mission. *Geophys. Res. Lett.* **35**, L03817 (2008).
20. Luo, S., Wang, D. & Flanagan, T. B. Thermodynamics of hydrogen in fcc Pd–Au alloys. *J. Phys. Chem. B* **114**, 6117–6125 (2010).
21. Nugroho, F. A. A., Iandolo, B., Wagner, J. B. & Langhammer, C. Bottom-up nanofabrication of supported noble metal alloy nanoparticle arrays for plasmonics. *ACS Nano* **10**, 2871–2879 (2016).
22. Nugroho, F. A. A., Darmadi, I., Zhdanov, V. P. & Langhammer, C. Universal scaling and design rules of hydrogen-induced optical properties in Pd and Pd-alloy nanoparticles. *ACS Nano* **12**, 9903–9912 (2018).
23. Mayer, K. M. & Hafner, J. H. Localized surface plasmon resonance sensors. *Chem. Rev.* **111**, 3828–3857 (2011).
24. Fukai, Y. *The Metal–Hydrogen System* (Springer, 1993).
25. Zorić, I., Larsson, E. M., Kasemo, B. & Langhammer, C. Localized surface plasmons shed light on nanoscale metal hydrides. *Adv. Mater.* **22**, 4628–4633 (2010).
26. Li, G. et al. Hydrogen storage in Pd nanocrystals covered with a metal–organic framework. *Nat. Mater.* **13**, 802–806 (2014).
27. Ngene, P. et al. Polymer-induced surface modifications of Pd-based thin films leading to improved kinetics in hydrogen sensing and energy storage applications. *Angew. Chem. Int. Ed.* **53**, 12081–12085 (2014).
28. Pivak, Y., Schreuders, H., Slaman, M., Griessen, R. & Dam, B. Thermodynamics, stress release and hysteresis behavior in highly adhesive Pd–H films. *Int. J. Hydrogen Energy* **36**, 4056–4067 (2011).
29. Yoo, H.-W., Cho, S.-Y., Jeon, H.-J. & Jung, H.-T. Well-defined and high resolution Pt nanowire arrays for a high performance hydrogen sensor by a surface scattering phenomenon. *Anal. Chem.* **87**, 1480–1484 (2015).
30. Yang, F., Kung, S.-C., Cheng, M., Hemminger, J. C. & Penner, R. M. Smaller is faster and more sensitive: the effect of wire size on the detection of hydrogen by single palladium nanowires. *ACS Nano* **4**, 5233–5244 (2010).
31. Koo, W.-T. et al. Accelerating palladium nanowire H₂ sensors using engineered nanofiltration. *ACS Nano* **11**, 9276–9285 (2017).
32. Delmelle, R., Ngene, P., Dam, B., Bleiner, D. & Borgschulte, A. Promotion of hydrogen desorption from palladium surfaces by fluoropolymer coating. *ChemCatChem* **8**, 1646–1650 (2016).
33. Nanba, Y., Tsutsumi, T., Ishimoto, T. & Koyama, M. Theoretical study of the hydrogen absorption mechanism into a palladium nanocube coated with a metal–organic framework. *J. Phys. Chem. C* **121**, 14611–14617 (2017).
34. Langhammer, C., Zhdanov, V. P., Zorić, I. & Kasemo, B. Size-dependent kinetics of hydriding and dehydriding of Pd nanoparticles. *Phys. Rev. Lett.* **104**, 135502 (2010).
35. Jeon, K.-J. et al. Air-stable magnesium nanocomposites provide rapid and high-capacity hydrogen storage without using heavy-metal catalysts. *Nat. Mater.* **10**, 286–290 (2011).
36. Hong, J. et al. A highly sensitive hydrogen sensor with gas selectivity using a PMMA membrane-coated Pd nanoparticle/single-layer graphene hybrid. *ACS Appl. Mater. Interfaces* **7**, 3554–3561 (2015).
37. Min, K. E. & Paul, D. R. Effect of tacticity on permeation properties of poly(methyl methacrylate). *J. Polym. Sci. B* **26**, 1021–1033 (1988).
38. *ISO 26142: 2010. Hydrogen Detection Apparatus – Stationary Applications* (ISO, 2010).
39. Yamada, Y., Yamada, T., Tasaka, S. & Inagaki, N. Surface modification of poly(tetrafluoroethylene) by remote hydrogen plasma. *Macromolecules* **29**, 4331–4339 (1996).

Author contributions

F.A.A.N. and C.L. designed the experiments, analysed the data and wrote the manuscript. F.A.A.N. and I.D. fabricated the sensors. F.A.A.N. performed sensing measurements on PTFE sensors. F.A.A.N. and I.D. performed sensing measurements on PMMA and tandem sensors. L.C. and A.H. executed the DFT calculations. A.S.-A. performed the XPS analysis. H.S. deposited the PTFE thin films. L.J.B. and B.D. performed the XRD analysis. A.B.d.S.F. and J.B.W. performed the TKD analysis. S.K. performed the STEM-EDS analysis. T.J.A. performed the FDTD simulations. V.P.Z. contributed the theoretical analysis on the sensor kinetics and PTFE strain. B.D. and C.L. coined the initial idea. C.L. coordinated the project.

Competing interests

Additional information

Methods

Sensor fabrication. All sensors were fabricated according to the protocol reported in ref. [21], and the detailed description is reproduced here for completeness. Evaporation masks were fabricated using the standard hole-mask colloidal lithography process[40] on 1 × 1 cm² glass substrates (Borofloat, Schott Scandinavia), on TEM windows made in house following the procedure in ref. [41], on silicon wafer substrates and on QCM crystals (Laptech, SC-cut, 10 MHz fundamental frequency) pre-coated with 100 nm CVD-grown SiO_2 (PECVD, STS) on one of the Au electrodes. The steps of the mask fabrication were as follows. (1) Substrates were cleaned (by ultrasonic agitation for glass, silicon and QCM crystals and only by rinsing for the TEM windows in order to not break the membrane) consecutively in acetone, isopropanol and de-ionized water. (2) PMMA (MicroChem, 4 wt% diluted in anisole, $M_w = 950,000$) was spin-coated onto the substrates at 2,000 r.p.m. for 30 s (yielding a PMMA thickness of ~280 nm) followed by soft baking at 170 °C on a hotplate for 5 min. (3) Samples were subjected to a 5 s oxygen plasma (50 W, 250 mtorr, Plasma-Therm Batchtop RIE 95m) to enhance the hydrophilicity of the sample surface. (4) A polyelectrolyte solution (poly diallyldimethylammonium, $M_w = 200,000–350,000$, Sigma Aldrich, 0.2 wt% in Milli-Q water, Millipore) was pipetted on the surface of the samples and left to incubate for 40 s before rinsing in de-ionized water, creating a positively charged surface layer on the PMMA surface. (5) A suspension of negatively charged polystyrene beads (PS, 190 nm sulfate latex, Interfacial Dynamics Corporation, 0.2 wt% in Milli-Q water) was added to the surface. The size of the PS beads determined the diameter of the fabricated nanodisks at the end of the processing. After 3 min incubation the suspension was rinsed away with dei-ionized water, and the samples were blown dry with nitrogen gas. (6) A 15-nm-thick Cr film was evaporated using a Lesker PVD 225 Evaporator at a base pressure of $5 × 10^{-7}$ torr and evaporation rate of 1 Å s⁻¹. (7) The PS beads were removed by tape stripping (SWT-10, Nitto Scandinavia) for glass, silicon and QCM samples and by a wet tissue for TEM windows. This left a Cr film with holes at the positions of the stripped PS beads. (8) The samples were subjected to 5 min oxygen plasma treatment (50 W, 250 mtorr, Plasma-Therm Batchtop RIE 95m) to etch through the PMMA layer exposed beneath the holes in the Cr mask. (9) Through this mask, Pd was deposited at a deposition rate of 1 Å s⁻¹. To fabricate the PdAu alloys, Au and Pd were deposited in sequence at the same deposition rate through the mask in tailored amounts. The thicknesses of each Au and Pd layer determined the final composition of the alloy particles. (10) The remaining PMMA layer was dissolved in acetone in a liftoff step, removing the mask from the sample and leaving only the nanodisk structures on the substrate. (11) Samples were soaked in isopropanol and blown dry with nitrogen. (12) Both Pd and Au–Pd samples were annealed in a home-made flow furnace under 4% H_2 in Ar (100 ml min⁻¹) at 500 °C for 24 h, except for samples on QCM crystals, which were annealed instead at 400 °C for 72 h to avoid α–β phase transformation in quartz at 450 °C, which leads to cracking. In this way, alloying of PdAu samples was achieved.

PTFE deposition. Thin PTFE films were prepared at room temperature in an ultrahigh-vacuum (UHV) d.c./radiofrequency magnetron sputtering system with a base pressure of 10^{-7} mbar and a deposition pressure of $5 × 10^{-3}$ mbar Ar[42]. The deposition rate was first determined by sputtering the target independently at a fixed power over a well-defined time interval. The thickness of the reference film was then measured with a DekTak3 profilometer, and the deposition rate (nm s⁻¹) was calculated from the thickness and time.

PMMA deposition. PMMA (MicroChem, 1 wt% diluted in anisole, $M_w = 950,000$) was spin-coated on sensors at 2,000 r.p.m. for 30 s followed by a soft baking at 170 °C on a hotplate for 5 min, resulting in a 35 nm PMMA film, as measured by ellipsometry (J.A. Woollam M2000). To enable spin-coating on an already PTFE-coated sensor to create the tandem structure, a hydrogen plasma treatment was applied for 5 s (100 W, 250 mtorr, Plasma-Therm Batchtop RIE 95m). This step rendered the PTFE surface hydrophilic and thus allowed spin-coating of PMMA onto it. The PMMA deposition steps were as described above.

Material characterization. All SEM images were obtained in a Zeiss Supra 60 VP with a secondary electron detector, working distance of 4 mm and an electron beam acceleration voltage of 10–15 kV. Scanning transmission electron microscopy (STEM) and energy dispersive X-ray spectroscopy (EDS) measurements were taken using an FEI Titan TEM instrument operated at 300 kV acceleration voltage. The electron probe diameter and convergence semi-angle were approximately 0.15 nm and 17.5 mrad, respectively. High-angle annular dark-field–STEM images were recorded with a collection semi-angle of approximately 47 mrad. EDS maps were obtained with a pixel size of ~5 nm and acquisition time of 1 s per pixel. The EDS maps were analysed in Aztec 3.3 (Oxford Instruments). The TKD investigation of the samples was performed on an FEI Nova Nano Lab 600 SEM equipped with Bruker Optimus TKD detector operated at an acceleration voltage of 30 kV and beam current of 1.7 nA using an aperture of 30 µm. The electron-transparent TEM window containing the nanoparticles was positioned horizontally on the microscope with the particles facing downward, and TKD orientation maps were acquired over a large number of particles with a scan step of 5 nm and exposure time of approximately 9 ms per point with a pattern resolution of

320 × 240 pixels (5 × 5 binning). High-resolution XPS spectra were recorded with a PHI 5000 system (Physical Electronics) using monochromatized Al Kα radiation ($hv\frac{1}{4}$ 1,486.6 eV) as the X-ray source. The high-resolution spectra displayed here were obtained at an incidence angle of 45° with a combined energy resolution of 0.01 eV. Atomic sensitivity factors for quantitative analysis were taken from a ref. [43]. The binding energies were corrected according to the Au 4f peak (84 eV) and the C 1s peak (284.8 eV). The Au 4f peak was also employed to correct for any additional charge build during high-resolution XPS measurements. For all measurements, the samples were electrically grounded to prevent accumulation of electrostatic charge. AFM measurements were performed in tapping mode using an SPM Bruker Dimension 3100 system in air. In situ XRD measurements were performed with a Bruker D8 Advance (Co-Kα $λ = 0.1789$ nm) equipped with an LYNXEYE 1D detector. During the XRD measurements, the sample was hydrogenated at a constant temperature of 25 °C inside an Anton Paar XRK 900 reactor chamber. As the loading gas, a mixture of 96.0% He and 4.0% H_2 was used and a constant flow of at least 20 s.c.c.m. was maintained at all times. After setting and reaching a new pressure set point, we waited 10 min before commencing the XRD measurements to make sure that the sample fully responded to the new experimental conditions. The XRD diffractograms were background-corrected by subtracting the diffractogram of an empty substrate. The values for the d111-spacing (the out-of-plane direction of the film) and the full-width at half-maximum were obtained from the best fit of a pseudo-Voigt function to the background-corrected experimental data. The rocking curves were collected around the <111> diffraction peak with a Bruker D8 Discover diffractometer (Cu-Kα, $λ = 0.1541$ nm). This diffractometer was also used for the ex situ XRD measurements. For Fourier transform infrared spectroscopy (FTIR), a Bruker IFS66 spectrometer with KBr windows was used. The samples were mounted in a cell that could be pumped and filled with hydrogen at room temperature. A 200 nm PTFE layer was sputtered on a 10 nm Pd film on a KBr substrate. The films were measured in the as-deposited state and after exposure to hydrogen for 10 min.

Hydrogen sensing measurements. For hydrogenation isotherm, kinetics and LoD measurements, all isotherm and kinetics measurements were performed in an home-made vacuum chamber set-up with optical windows, as reported earlier[4,21]. The absolute hydrogen pressure in the chamber was monitored using two capacitive pressure gauges with different ranges (MKS Baratron). Optical transmittance measurements through the sample were enabled by UHV-compatible sapphire windows mounted on the vacuum chamber, and by using a fibre-coupled, unpolarized white light source (AvaLight-Hal, Avantes) and a fixed-grating fibre-coupled spectrophotometer (SensLine AvaSpec-2048XL, Avantes). The pressure inside the chamber was controlled using a microbar-precision leak valve. The temperature was maintained with a heating coil wrapped around the chamber and a temperature controller (Eurotherm 3216N) in a feedback loop manner, where the sample surface temperature inside the vacuum chamber was continuously used as input. All experiments were performed at constant 30 °C. The LoD measurements were performed at 1 Hz sampling frequency (0.165 ms integration time with 1,000 averages). The kinetics measurements were performed at a frequency of 6 Hz (0.165 ms integration time with 10 averages). The observed higher noise in the kinetics data is thus a consequence of the lower number of averaged spectra per data point (Supplementary Figs. 22 and 23). It is also important to note that the apparent sampling frequency obtained by the set-up is slower than the theoretical one (that is, integration time × averaging number) due to the delay in the computing system when acquiring, processing, analysing and plotting the data in real time. The LSPR peak descriptors were obtained by fitting a Lorentzian function to the wavelength range at ±60 nm around the LSPR peak in the measured optical extinction spectra, within which a good fit ($R^2 > 0.95$) is obtained, despite the asymmetry of the global LSPR peak (Supplementary Fig. 19). In the experiments to determine the apparent activation energies, absorption and desorption kinetics measurements to and from 900 mbar were performed at four different temperatures (30–60 °C, in 10 °C steps). For the Arrhenius analysis, t_{50} was used as a measure of the process rate. For the long-term stability test, we stored the Pd sensors under controlled ambient conditions (average temperature 21.2 °C, humidity 23% relative humidity, CO_2 323 ppm). We also performed the test on pure Pd sensors (and not on the $Pd_{70}Au_{30}$ alloy) for two reasons. First, the neat Pd sensor exhibits a much slower response than the analogue $Pd_{70}Au_{30}$ and thus its kinetics can be resolved in more detail so that any variation due to measurement artefacts can be minimized. Second, neat Pd is significantly more prone to poisoning than PdAu (Supplementary Fig. 49), which makes it a more effective system for investigating the long-term stability of a polymer coating with respect to preventing sensor deactivation. For deactivation and poisoning tests and LoD measurements in Ar and air, the deactivation and LoD measurements were carried out in a quartz tube flow reactor at atmospheric pressure with optical access for transmittance measurements (X1, Insplorion AB), using synthetic air as the carrier gas, as well as Ar for the LoD experiment[44]. The gas flow rate (kept constant at 100 and 500 or 325 ml min⁻¹, for deactivation and LoD measurements in Ar and air, respectively) and gas composition were regulated by mass flow controllers (Bronkhorst ΔP). The sample inside the flow reactor was illuminated by white light (AvaLight-Hal, Avantes) through an optical fibre equipped with a collimating lens. The transmitted light was then analysed using a fibre-coupled fixed-grating

spectrometer (AvaSpec-1024, Avantes; or SensLine AvaSpec-2048XL, Avantes, for LoD measurements). The measurement temperature was maintained at 30 °C. For QCM measurements the QCM window module (QSense Explorer Microscopy, Biolin Scientific Corporation) was connected to a series of mass flow controllers (Bronkhorst ΔP) to regulate the H_2 partial pressure in Ar carrier gas at a constant total flow rate of 30 ml min^{-1}. Data collection was carried out with QSoft (Biolin Scientific). The absorbed hydrogen content in the nanoparticles was calculated from the QCM frequency shift via the Sauerbrey equation[45] and analysis of the nanoparticle surface coverage based on SEM images of the crystal, as described in detail elsewhere[22]. All measurements were carried out at 30 °C.

DFT calculations. All the modelled structures were optimized within the DFT framework. The cluster models were optimized using the PBE functional[46] while van der Waals contributions were included for the polymer and polymer–H_2 systems by using the vdW-CX functional[47]. Geometry optimizations were performed using the Vienna ab initio simulation package, VASP[48,49]. Projector augmented waves (PAW)[50,51] were used, with a plane-wave kinetic energy cutoff of 500 eV. To avoid artificial interaction due to the periodic boundary conditions, a $30 \times 30 \times 31$ Å^3 supercell was used, ensuring at least 16 Å of vacuum between two successive images. Γ-centered[52] calculations were performed with a Gaussian smearing, σ, of 0.02 eV, with the energies extrapolated to $\sigma = 0.00$ eV. The atom positions were optimized until meeting the criterion of the residual forces on any direction being less than 0.02 eV Å^{-1}.

FDTD simulations. We used FDTD Solutions (Lumerical Inc., Canada) to calculate the optical spectra of a Pd nanodisk as a function of the refractive index of the coating and the coating thickness. Due to the fact that the fabricated arrays are amorphous in terms of the nanoparticle arrangement on the surface, we cannot model exactly the whole sensor and accordingly are limited to either a single disk or, to account for interparticle coupling, a periodic lattice. In the present case we first chose the former solution, although in one case we also considered a hexagonal lattice. The Pd nanodisk was modelled with a diameter of 180 nm, 30 nm thickness and rounded edges. The permittivities of Pd and Pd hydride (PdH$_{0.67}$) are taken from the literature[53]. The structures were placed directly on top of a glass substrate ($n = 1.45$) and were conformally coated by an isotropic dielectric layer with a variable thickness and refractive index. In the simulations the thickness was in the range 5–75 nm and the refractive index in the range 1–1.6. This included the range of parameters considered in the experiment. The structures were illuminated by a plane wave and extinction was collected and analysed in terms of resonance position.

Data avaibility

All experimental data within the article and its Supplementary Information are available from the corresponding authors upon reasonable request.

References

40. Fredriksson, H. et al. Hole–mask colloidal lithography. *Adv. Mater.* **19**, 4297–4302 (2007).
41. Grant, A. W., Hu, Q.-H. & Kasemo, B. Transmission electron microscopy windows for nanofabricated structures. *Nanotechnology* **15**, 1175–1181 (2004).
42. Slaman, M., Westerwaal, R., Schreuders, H. & Dam, B. Optical hydrogen sensors based on metal-hydrides. *Proc. SPIE* **8368**, 836805 (2012).
43. Briggs, D. & Seah, M. P. *Practical Surface Analysis, Auger and X-ray Photoelectron Spectroscopy* (Wiley, 1990).
44. Nugroho, F. A. A. et al. Plasmonic nanospectroscopy for thermal analysis of organic semiconductor thin films. *Anal. Chem.* **89**, 2575–2582 (2017).
45. Sauerbrey, G. Verwendung von Schwingquarzen zur Wägung dünner Schichten und zur Mikrowägung. *Zeitschrift für Phys.* **155**, 206–222 (1959).
46. Perdew, J. P., Burke, K. & Ernzerhof, M. Generalized gradient approximation made simple. *Phys. Rev. Lett.* **77**, 3865–3868 (1996).
47. Berland, K. & Hyldgaard, P. Exchange functional that tests the robustness of the plasmon description of the van der Waals density functional. *Phys. Rev. B* **89**, 035412 (2014).
48. Kresse, G. & Furthmüller, J. Efficiency of ab-initio total energy calculations for metals and semiconductors using a plane-wave basis set. *Comput. Mater. Sci.* **6**, 15–50 (1996).
49. Kresse, G. & Furthmüller, J. Efficient iterative schemes for ab initio total-energy calculations using a plane-wave basis set. *Phys. Rev. B* **54**, 11169–11186 (1996).
50. Blöchl, P. E. Projector augmented-wave method. *Phys. Rev. B* **50**, 17953–17979 (1994).
51. Kresse, G. & Joubert, D. From ultrasoft pseudopotentials to the projector augmented-wave method. *Phys. Rev. B* **59**, 1758–1775 (1999).
52. Monkhorst, H. J. & Pack, J. D. Special points for Brillouin-zone integrations. *Phys. Rev. B* **13**, 5188–5192 (1976).
53. Silkin, V. M., Díez Muĩo, R., Chernov, I. P., Chulkov, E. V. & Echenique, P. M. Tuning the plasmon energy of palladium-hydrogen systems by varying the hydrogen concentration. *J. Phys. Condens. Matter* **24**, 104021 (2012).